Confinement of Dirac electrons in graphene quantum dots

Wouter Jolie,[1] Fabian Craes,[1,*] Marin Petrović,[2] Nicolae Atodiresei,[3] Vasile Caciuc,[3] Stefan Blügel,[3] Marko Kralj,[2]
Thomas Michely,[1] and Carsten Busse[1]

[1]*II. Physikalisches Institut, Universität zu Köln, Zülpicher Straße 77, 50937 Köln, Germany*

[2]*Institut za fiziku, Bijenička 46, 10000 Zagreb, Croatia*

[3]*Peter Grünberg Institut (PGI) and Institute for Advanced Simulation (IAS), Forschungszentrum Jülich and JARA, 52425 Jülich, Germany*

We observe spatial confinement of Dirac states on epitaxial graphene quantum dots with low-temperature
scanning tunneling microscopy after using oxygen as an intercalant to suppress the surface state of Ir(111)
and to effectively decouple graphene from its metal substrate. We analyze the confined electronic states with
a relativistic particle-in-a-box model and find a linear dispersion relation. The oxygen-intercalated graphene
is p doped [$E_D = (0.64 \pm 0.07)$ eV] and has a Fermi velocity close to the one of free-standing graphene
[$v_F = (0.96 \pm 0.07) \times 10^6$ m/s].

I. INTRODUCTION

Quantum dots are nanostructures that are small enough
to induce quantum-size effects to electronic states: The
confinement induced by them splits the continuous distribution
of energy E and momentum k into discrete, atomlike states.
Of specific interest in this respect are graphene quantum
dots (GQDs) as they could form spin qubits due to the
long spin coherence time in graphene [1]. Recently, it has
been shown that also plasmons can be confined in graphene
nanostructures [2,3]. In scanning tunneling spectroscopy
(STS) confinement effects of electronic states can be observed
as discrete peaks in the local density of states (LDOS) and
by spatial mapping of the respective eigenstates that can be
viewed as a standing wave pattern of scattered electrons or
holes [4].

Recently, several STS studies showed that GQDs epitaxially
grown on Ir(111) can indeed induce confinement [5–7].
Although it is tempting to assign these states to the Dirac
states of graphene (gr), several issues are puzzling: In Ref. [5]
the size-dependent energies of the first and second states
were attributed to the characteristic linear dispersion relation
of graphene with a Fermi velocity of $v_F = 10^6$ m/s in
agreement with angle-resolved photoemission spectroscopy
(ARPES) [8], whereas substantially lower values of $v_F \approx
0.6 \times 10^6$ m/s are deduced in Refs. [6,7]. In addition, for the
latter studies a slight n-doping of graphene is found, in contrast
to the p doping established for extended graphene [9]. To
make things worse, the most recent study [10] questions the
assignment of these states to the Dirac electrons, but rather
interprets them as the confined Ir(111) surface state S_0 at
the Γ point which persists underneath graphene [11,12]. This
hypothesis was also put forward in Ref. [5] for the case of
large islands.

The results of the existing literature can be compared when
the data are analyzed in a standardized way: To determine
the wave vector k belonging to a state with specific E we
approximate a GQD with an area A as an infinite cylindrical
well with radius $r = \sqrt{A/\pi}$. In this case, the wave functions of

a confined state in polar coordinates (ρ,ϕ) are given by $\Psi_{m,l}
\propto J_l(k_{m,l}\rho)e^{\pm il\phi}$, where J_l is the spherical Bessel function
of the first kind with order l [4]. Due to the confinement,
$\Psi_{m,l}$ must have a node for $\rho = r$, leading to the condition
$k_{m,l}r = z_{m,l}$ with $z_{m,l}$ the mth zero of J_l, and so the eigenstates
are labeled (m,l). STS is sensitive to the LDOS $= \Psi_{m,l}^*\Psi_{m,l} \propto
J_l^2(k_{m,l}\rho)$, so the dependence on ϕ vanishes. In general, the
index m gives the number of maxima in the LDOS with
respect to ρ; the eigenstates with $l = 0$ have a maximum in
the center of the well, whereas states with higher l have a
minimum in the center and the first maximum moves outward
with increasing l. Less abstract, the $(1,0)$ state looks like a
bubble, $(1,1)$ looks like a ring, and $(2,0)$ looks like a sombrero
[cf. the insets in Fig. 4(b), showing $\Psi_{m,l}^*\Psi_{m,l}$ for $(m,l) =
(1,0)$, $(1,1)$, and $(2,0)$, respectively]. Once we determined the
quantum numbers (m,l) of a given state at an energy E by
means of its shape, the momentum $k_{m,l}$ can be calculated via
$k_{m,l} = z_{m,l}/r = z_{m,l}\sqrt{\pi/A}$. Note that E and k are obtained
independently, without any assumption about the dispersion
relation.

Figure 1 shows the result of this analysis for the published
data. The value from Ref. [5] [cf. Fig. 3(h) therein] can directly
be transformed into a relation $E(A)$, and with A we can
deduce $k_{m,l}$ for states with known (m,l) [note that $n = 0$
and $n = 1$ in Ref. [5] are $(1,0)$ and $(1,1)$ in our notation,
respectively] [13]. For the case of Ref. [6], Fig. 3(a) contains
data of the scanning tunneling microscopy (STM) sample
bias where state S [corresponding to $(1,0)$ in our notation]
is observed vs island area A. Also here we get $k_{m,l}$ using A
and the quantum numbers of the respective state, the energy
E is determined by the bias voltage. Reference [7] already
presents the data in the form $E(k)$ (Fig. 4). Finally, we convert
the peak position vs (diameter)$^{-2}$ plot in Fig. 3(e) from Ref.
[10] into $E(k)$ using the Bessel-type analysis. For comparison,
we also include the two dispersion relations for the extended
system as determined by ARPES. The black line is $E(k)$
for the Dirac states in graphene using $E_D = 0.1$ eV for the
position of the Dirac point and $v_F = 10^6$ m/s for the Fermi
velocity [8,14]. The red line is the spin-averaged Ir(111)
S_0 surface state underneath graphene [11]. It is obtained by
fitting a polynomial up to order $n = 8$ using only even n
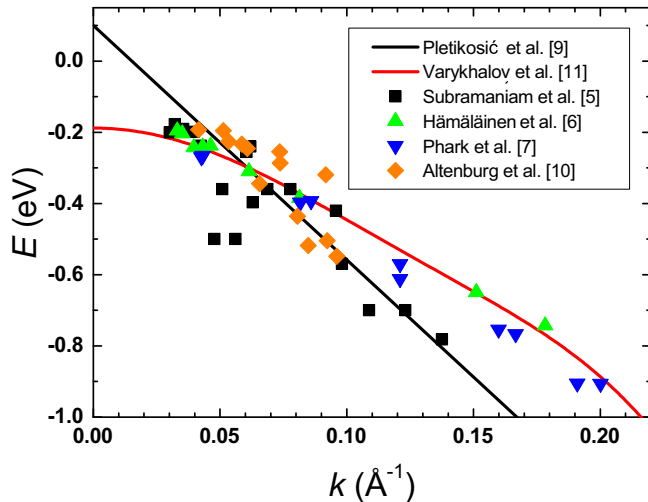
*craes@ph2.uni-koeln.de

FIG. 1. (Color online) Overview of the existing literature data on gr/Ir(111): Lines represent ARPES measurements on extended systems; the symbols represent data on small graphene islands.

to each of the two spin-split branches of the ARPES data. We averaged the two branches as this corresponds to the bands obtained by STM analysis of scattering patterns in Rashba-split systems, since scattering can only take place within the same branch as spin conservation has to be obeyed [15].

It is obvious that based on this data alone it is not possible to attribute any of the experiments unambiguously to the Dirac states or the Ir(111) surface state. This can also be quantified by calculating the root-mean-square deviation of all four data sets with respect to the two models: The data from Refs. [6,7] fit much better to the surface state S_0 than to the Dirac dispersion, whereas the data from Refs. [5,10] are described by both models equally well. It is also peculiar that there exists no data above the maximum energy of the surface state. One can conclude that the coexistence of the Dirac states of graphene and the surface state of Ir(111) does not allow a clear assignment of the experimentally observed standing wave patterns.

At first sight it is surprising that it is not possible to clearly distinguish between Dirac states at the K points with a linear dispersion and a Rashba-split near-parabolic surface state with negative effective mass [11]. The reasons for this are that (i) the standing wave patterns observed in STM are only determined by the differences between in- and outgoing waves and are, in consequence, insensitive to the absolute values of the k vectors involved; (ii) the Rashba-splitting is averaged out in STM observations [15] because scattering is only allowed between states with the same spin quantum number; and (iii) the curvature of the near-parabolic S_0 is rather low in the analyzed range of energies (in fact, just fitting a line to the spin-averaged S_0 in the range between 0.05 Å^{-1} and 0.2 Å^{-1} yields $v_F = 0.6 \times 10^6$ m/s, disturbingly close to the value determined in Refs. [6,7]).

The most clear-cut way to resolve this situation is to prepare a system where the surface states of Ir(111) are absent. In this paper we demonstrate that this goal can be achieved using intercalation of oxygen [16,17]. This leaves

Dirac states as the only explanation for the eigenstates we observe.

II. METHODS

STM/STS is performed at a temperature $T = 5$ K and a pressure $p < 10^{-11}$ mbar, ARPES at $T = 150$ K, and $p < 5 \times 10^{-10}$ mbar. For STS, we measure the dI/dV signal which represents the LDOS of the sample after normalization by I/V (V is the voltage applied to the sample and I is the resulting tunneling current through the tungsten tip) [18]. We use a lock-in technique with a frequency in the range of 850–950 Hz and a modulation amplitude of $V_{mod} \leqslant 10$ mV, resulting in a lower limit of the experimental resolution of $\Delta E \approx \sqrt{(3.3k_B T)^2 + (1.8eV_{mod})^2} \leqslant 0.02$ eV [19]. Some of the recorded STM images are analyzed with WsXM [20]. A helium discharge lamp ($\hbar\omega = 21.2$ eV) is used for excitation in ARPES and a Scienta SES 100 analyzer (25 meV energy resolution, $0.2°$ angular resolution) for data acquisition. For better visibility, the derivative of the photoemission intensity is shown in some of our spectra [dashed rectangles in Figs. 2(c) and 2(d)]; i.e., the data appears as illuminated from below with the bright states casting dark shadows.

The sample is prepared at $p < 5 \times 10^{-10}$ mbar. The Ir(111) single crystal is cleaned by cycles of Ar$^+$ ion bombardment, exposure to oxygen at 1120 K and annealing at $T \geqslant 1500$ K. We apply temperature-programed growth (TPG) of graphene [21], adsorbing ethylene as a precursor at room temperature followed by annealing at $T \gtrsim 1300$ K. For the STM experiment, we used one TPG step as this leads to GQDs with sizes where sufficiently separated discrete states are expected. For the ARPES measurements we used six cycles followed by chemical vapor deposition (CVD) using ethylene with $p = 10^{-7}$ mbar at 1120 K for 5 min, leading to nearly full coverage. Thereby, we (i) obtain a high photoemission intensity from graphene and (ii) achieve a low density of graphene step edges which are known to scatter Ir surface states and thus reduce their photoemission intensity [8]. To achieve oxygen intercalation, the sample is exposed to more than 750 L of O$_2$ at $T \geqslant 450$ K, exceeding the amount for saturation coverage by more than an order of magnitude [16]. The intercalated oxygen forms a (2×1) structure with respect to Ir(111), as evidenced by the low-energy electron diffraction (LEED) pattern shown in Fig. 2(g) and STM (see Fig. 5), in agreement with previous work [16]. Note that the LEED pattern resembles a (2×2) structure with respect to Ir(111) because three rotational domains of (2×1) are present on the surface.

First-principles calculations have been performed in the framework of density functional theory (DFT) [22,23] as implemented in VASP [24,25], using the projector augmented plane-wave (PAW) method [26] to describe the interaction between the valence electrons and the atomic cores and the Perdew-Burke-Ernzerhof (PBE) exchange-correlation functional [27]. To describe the long-range nonlocal correlation effects responsible for the van der Waals interaction we applied the semiempirical DFT-D2 method [28]. The gr/O/Ir(111) system was modeled by a large realistic supercell consisting of 1129 atoms. The plane-wave cutoff energy was set to 500 eV.
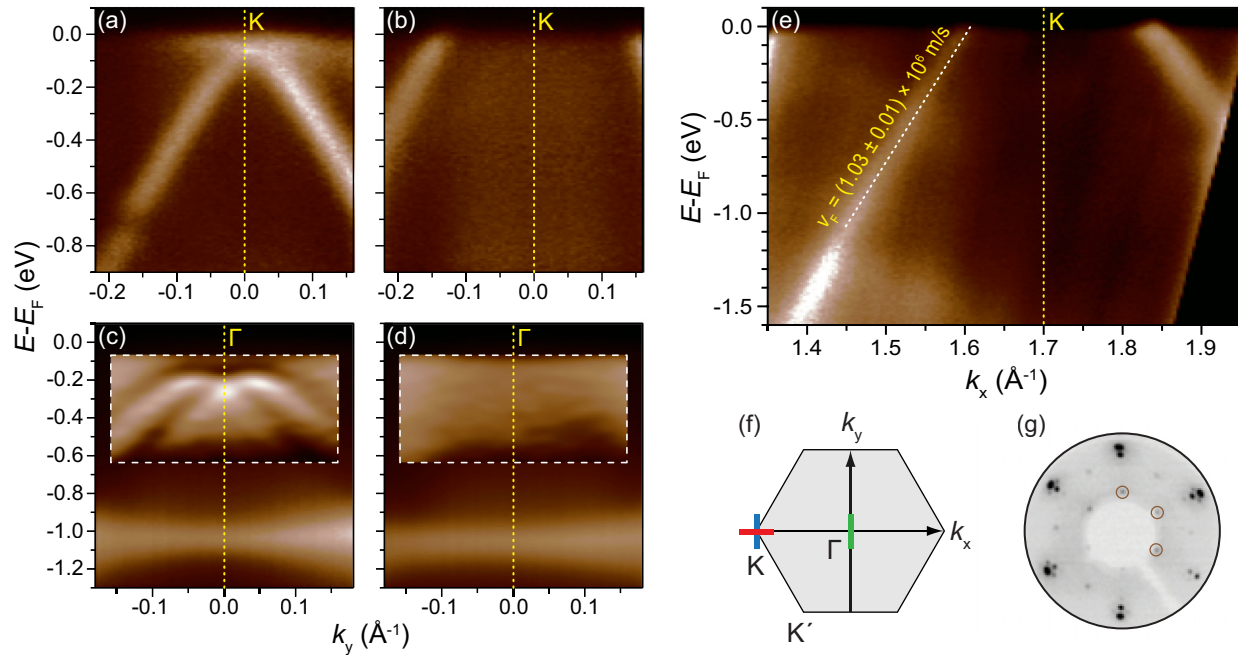
FIG. 2. (Color online) ARPES spectra of graphene on Ir(111) before (a),(c) and after (b),(d),(e) oxygen intercalation. (a)→(b) K-point, measured along the vertical line at K sketched in (f): The Dirac cone of graphene shifts to higher energies due to p-doping after oxygen intercalation. (c) → (d) Γ point, measured along the vertical line at Γ in (f): The Rashba-split Shockley surface state is visible before oxygen intercalation, but not afterwards. The contrast is enhanced inside the dashed rectangles in order to optimize the visibility of the iridium surface state. (e) ARPES spectra of gr/O/Ir(111) measured along the horizontal line at K in (f). The dispersion relation resulting from the fit is marked by the white dotted line. (f) First Brillouin zone of graphene with three lines representing the paths of the recorded spectra perpendicular to ΓK at K [(a),(b)] and Γ [(c),(d)], as well as along ΓK at K [(e)]. (g) LEED image (inverted contrast) of gr/O/Ir(111) obtained at 60 eV. The enclosed spots are periodicities of the three $60°$-rotated oxygen (2×1) structures.

III. RESULTS AND DISCUSSION

The global band structure of gr/Ir(111) and gr/O/Ir(111) is determined using ARPES (note that it is not possible to measure confinement effects in ARPES due to the size distribution of the GQDs). The spectra shown in Figs. 2(a)–2(d) are acquired in a direction perpendicular to ΓK, while Fig. 2(e) is recorded along the ΓK direction. This is visualized in Fig. 2(f) with a blue line for (a) and (b), a green line for (c) and (d) and a red line for (e). For gr/Ir(111), the characteristic linear dispersion of graphene at the K point is observed [Fig. 2(a)], as is well known from other experiments [8,9]. At the Γ point, the Rashba-split near-parabolic Ir(111) surface state S_0 with negative effective mass is visible (Fig. 2(c), see also Refs. [11,12]). The intercalation of oxygen shifts the Dirac point up in energy (Fig. 2(b); see also Ref. [17]). The surface state S_0 is not visible anymore [Figs. 2(d)], in agreement with the strong suppression of surface states on other close-packed metal surfaces after adsorption of oxygen; see, e.g., Refs. [29–31]. In addition, there is no indication of the S_1 state at the K point [9]. The dominant intensity below 1 eV remains in Fig. 2(d), as it belongs to direct transitions from bulk Ir bands [14].

Figure 2(e) shows additional ARPES results for oxygen-intercalated graphene on Ir(111). In contrast to the preparation described in Sec. II, here the process is stopped after six TPG cycles as the presence of many graphene edges is not as critical for the electronic states of graphene as it is for the Ir(111) surface states. As mentioned above, these results

are obtained *in* the ΓK direction [see red line in Fig. 2(f)], thus allowing us to cover an extended k range of the Dirac cone. We determine the relation $E(k)$ by first fitting the peak positions (single Lorentzian) of individual momentum distribution curves (MDCs) of the left branch of the Dirac cone and then fitting the linear function $E(k) = E_D - \hbar v_F k$ to these peak positions in the energy range between -1 and -0.2 eV. With this range a reliable fit is obtained, avoiding narrow energy-range disturbances as the electron-phonon coupling kink (near to E_F) or π-band intensity variations (below -1 eV). We obtain the parameters $E_D = (0.68 \pm 0.05)$ eV and $v_F = (1.03 \pm 0.01) \times 10^6$ m/s.

The main outcome of our calculations is summarized in Fig. 3. Panel (a) shows the supercell, containing (20×10) unit cells of graphene adsorbed on (9×9)O/(18×9)Ir(111). For comparison, we also show the pristine gr/Ir(111) [Fig. 3(b); note that here the supercell is smaller]. The average binding distance between graphene and Ir(111) is $\bar{h} = 4.23$ Å [see also Fig. 3(d)], which is larger than without O ($\bar{h} = 3.41$ Å, Fig. 3(e) and Ref. [32]). The peak-to-peak corrugation drops from $\Delta h = 0.35$ Å without O to $\Delta h = 0.19$ Å for intercalated O. Figure 3(c) shows the PDOS of the graphene π orbitals: Ideal (i.e., planar and free-standing) graphene is shown as the gray-filled area. At the Fermi energy the characteristic dip due to the Dirac point is visible. Also for free-standing graphene in the slightly corrugated geometry as found for gr/O/Ir(111) [green (light gray) line] the overall shape is preserved and the Dirac point coincides with the Fermi energy. However,
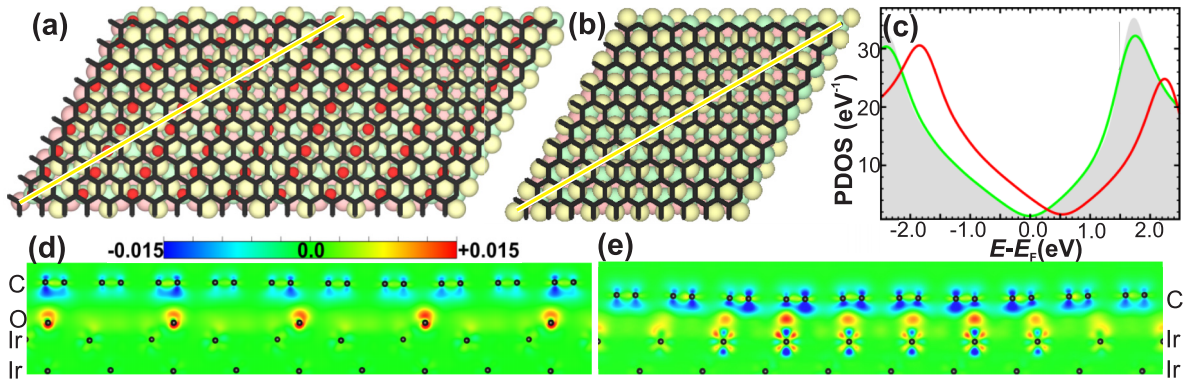
FIG. 3. (Color online) (a) Top view of gr/O/Ir(111) [(20×10)gr/(9×9)O/(18×9)Ir(111)]. (b) Top view of gr/Ir(111) [(10×10)gr/(9×9)Ir(111)]. (c) Projected density of states (PDOS) in states/eV of the graphene π-like orbitals. Gray area, free-standing graphene; green line (light gray), free-standing graphene with the same shape as found for gr/O/Ir(111); red (dark gray) line, gr/O/Ir(111). (d) Charge density difference upon adsorption for gr/O/Ir(111) through a plane marked by the bright line in (a) (see color bar: negative values denote charge depletion; unit is $e\ \text{Å}^{-3}$). (e) Same as (d) for gr/Ir(111).

the adsorption of graphene on O/Ir(111) [red (dark gray) line] leads to a charge transfer and the Dirac cone is shifted to $E_D = 0.55$ eV, in good agreement with our ARPES experiments (see Fig. 2). The charge density difference plot [Fig. 3(d)] reveals the origin of this doping: Charge is transferred from the C π orbitals into the O/Ir(111) interface states. Note that no charge accumulation between C and O or Ir atoms takes place, which implies that no chemical bonds are formed. This is in contrast to gr/Ir(111), where at the fcc and hcp sites weak polar local covalent bonds are formed; see Fig. 3(e) and Ref. [32]. Taken together, the enlarged distance as well as the absence of hybridization between the graphene and the metal substrate indicate efficient decoupling, i.e., the absence of local bonding. A homogeneously charged graphene layer results.

STM reveals the presence of oxygen-intercalated GQDs of varying shape (hexagons, truncated hexagons, irregular polygons) and size [33]. An STM topography of an individual, slightly triangular GQD is shown in Fig. 4(b) (top left). Point spectra [Fig. 4(a)] are recorded at the locations indicated by the differently shaded dots. Pronounced peaks are visible in the spectra which we attribute to the discrete energies of the first three eigenstates on the graphene flake. The intensity of a given state varies with the location of the spectra on the GQD. This is most obvious in the images mapping the LDOS in Fig. 4(b) at energies approximately at the peak energies [indicated by blue (dark) vertical lines in Fig. 4(a)]. The characteristic standing wave patterns of confined states are visible.

We determined $E(k)$ from our STS results as explained above. First, we identify the experimentally observed states as (1,0) at 0.075 eV, (1,1) at -0.150 eV, and (2,0) at -0.425 eV by comparing them to our model (see insets). The recorded states do not always show an LDOS isotropy in ϕ [see, for
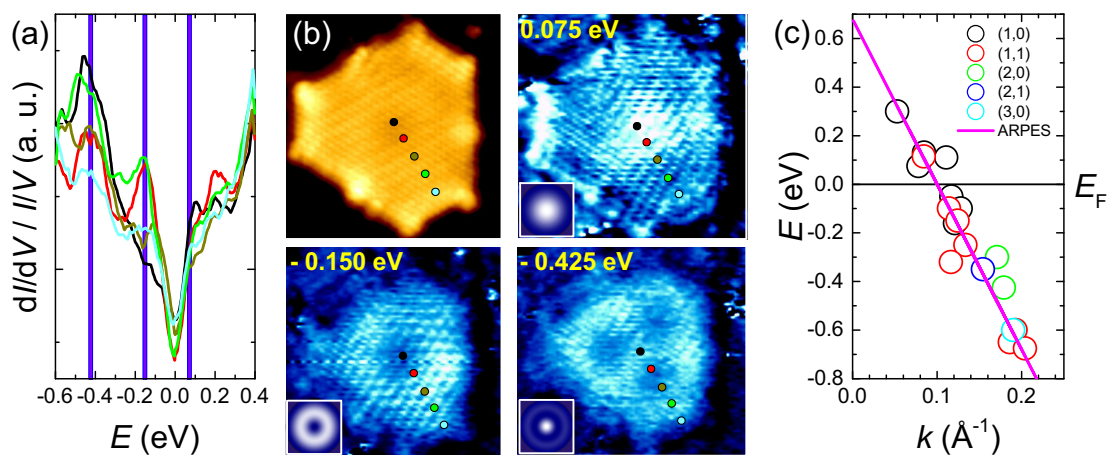

FIG. 4. (Color online) Confined states on a GQD. (a) dI/dV spectra recorded on graphene, revealing the energies of the confined states (stabilizing parameters are $I_{\text{stab}} = 0.4$ nA, $V_{\text{stab}} = 0.6$ V). (b) Topographic ($I = 0.1$ nA, $V = -0.150$ V, image size 75×77 Å^2) and spectroscopic images of the GQD, the latter measured at the three energies highlighted by three blue (dark) vertical lines in the spectra in (a), where the width of the lines corresponds to the experimental error evaluated above. The differently shaded dots indicate where the spectra were detected. The three states expected for a circular GQD are shown in the inset for comparison. (c) $E(k)$ resulting from the analysis of the confined states compared with the dispersion relation around the K point found in ARPES. The size of the dots corresponds to $\Delta E = \pm 0.05$ eV. A potential error of k due to our simplified model is neglected.

example, the state recorded at -0.425 eV in Fig. 4 (b)] since the real, noncircular shape of the GQD affects the form of the wave function [34]. Nevertheless, a clear characterization is possible for all our confined states. In a second step, we use the area A of the island to calculate $k_{m,l}$ for a known state (m,l). Finally, E can be determined from the STM bias voltage.

We obtained $E(k)$ via the identification of individual states either by mapping them at energies determined in point spectra [as for the example given in Figs. 4(a) and 4(b)] or from maps at closely spaced equidistant energies (not shown). We use this spacing as the maximum error $\Delta E = \pm 0.05$ eV, which is comparable to the full width at half maximum of our dI/dV spectra [see Fig. 4(a)] and not much larger than the lower limit of our experimental resolution. The enhanced broadening can arise from a finite (instead of infinite) potential well or Dirac-specific effects like Zitterbewegung [35]. A linear fit to the data in Fig. 4(c) (not shown) yields $E_D = (0.64 \pm 0.07)$ eV and $v_F = (0.96 \pm 0.07) \times 10^6$ m/s, which agrees remarkably well with the dispersion relation of the Dirac states determined by ARPES shown as a solid line in Fig. 4(c). It is also interesting to note that v_F is almost equal to the value for free-standing graphene, a strong indication for the decoupling of graphene as a consequence of the chosen intercalant [17].

The effective decoupling of graphene from the metal surface by the intercalated layer of O has further consequences: In Fig. 5(a) we compare point spectra taken on top of a GQD and next to it. The exact locations of the spectra are shown in the inset of the figure. On the GQD, a pronounced dip in the LDOS around 0.6 eV is observed, which we attribute to the vanishing density of states at the Dirac point of graphene. This feature was never observed on nonintercalated graphene on Ir(111), which we explain by the dominant contribution of the states at the Γ point from the metal in close proximity as compared
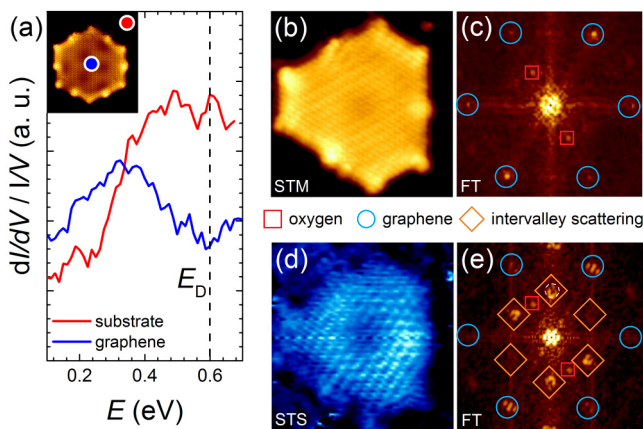
with the states of graphene at the K points that are furthermore suppressed by the large transfer of parallel momentum in the tunneling process [36].

Finally, we compare a topographic image of a GQD [Fig. 5(b)] and its Fourier transform (FT) [Fig. 5(c)] with the simultaneously acquired dI/dV map at $E = -0.150$ eV [Fig. 5(d)] and the corresponding FT [Fig. 5(e)]. In Fig. 5(c) several periodicities reveal themselves as peaks: The outermost spots (enclosed by circles) stem from the graphene lattice, while the two inner spots (enclosed by squares) are caused by one rotational domain of O in a (2×1) structure with respect to Ir(111) underneath graphene [compare Fig. 3(a)]. In the FT of the spectroscopic image [Fig. 5(e)], additional features appear, namely rings (enclosed by diamonds) centered at the $(\sqrt{3} \times \sqrt{3})R30°$ position (with respect to graphene), which, in consequence, have to be of electronic rather than structural origin. Specifically, this feature is markedly different from the crystallographic peaks observed for the case of graphene intercalated with O in a $(\sqrt{3} \times \sqrt{3})R30°$ structure [33]. Following previous studies, we propose that these rings arise from intervalley scattering between neighboring valleys around K and K' [37,38]. For the diameter of the ring one expects $d(E) = 4k(E)$ [38]. We superimposed a dashed white circle with the expected diameter based on $E(k)$ as determined using ARPES with one of the rings in Fig. 5(e). The agreement confirms our interpretation. The rings are most pronounced for scattering processes perpendicular to the O rows, which can be a hint at the underlying scattering mechanism. However, also the shape of the island is asymmetric, which may also induce intensity differences. Again, these electronic features are properties of decoupled graphene only and were never found for gr/Ir(111) without intercalated O. The diameter of the GQD in Fig. 5(b) is ≈ 100 Å, which implies that the k resolution in the corresponding FT is $\Delta k = \frac{2\pi}{100}$ Å$^{-1} \approx 0.06$ Å^{-1}, thus explaining the rather blurred appearance of the rings attributed to intervalley scattering in Fig. 5(e) and impeding a redundant determination of $E(k)$ via the analysis of scattering patterns. For this, much larger graphene sheets have to be analyzed [38], which is beyond the scope of this article focusing on GQDs. In addition, several satellite spots around the graphene spots and the central spot can be seen. However, it remains unclear whether they arise from intravalley scattering, from the symmetry of the $(1,1)$ state (compare Ref. [7]), or from the moiré pattern of gr/Ir(111), since they all yield similar reciprocal lengths.

IV. CONCLUSION

To summarize, we have extracted a linear dispersion relation with parameters matching those of Dirac states in oxygen-intercalated graphene as determined by ARPES. As the iridium surface states are destroyed by the presence of oxygen, their contribution can be completely excluded. In consequence, the states observed by us are the first unambiguous realization of confined Dirac states. Our study thus resolves the ambiguity of previous work and in consequence provides the first clear-cut demonstration of confinement of Dirac states. Furthermore, we observe the presence of intervalley scattering and a dip in the LDOS located at the Dirac point. The fact that all these effects are present underlines that intercalated oxygen renders graphene quasi-free-standing.

FIG. 5. (Color online) (a) dI/dV spectra taken on the substrate [red (light gray)] and on the GQD [blue (dark gray)] as shown in the inset ($I = 0.5$ nA, $V = 0.7$ V, image size 110×120 Å^2). On graphene, a dip is visible at ≈ 0.6 eV, which is absent on the substrate (stabilizing parameters are $I_{stab} = 0.05$ nA, $V_{stab} = 0.7$ V). (b) Same STM image as in Fig. 4 (b). (c) FT of (b), revealing the periodicities of graphene (enclosed by circles) and the intercalated oxygen rows forming a (2×1) structure (enclosed by squares). (d) Same dI/dV map of the $(1,1)$ state as shown in Fig. 4 (b). (e) FT of (d) containing additional features (enclosed by diamonds) arising from intervalley scattering.

ACKNOWLEDGMENTS

[1] B. Trauzettel, D. V. Bulaev, D. Loss, and G. Burkard, Nat. Phys. **3**, 192 (2007).

[2] J. Chen, M. Badioli, P. Alonso-González, S. Thongrattanasiri, F. Huth, J. Osmond, M. Spasenović, A. Centeno, A. Pesquera, P. Godignon, A. Z. Elorza, N. Camara, F. J. García de Abajo, R. Hillenbrand, and F. H. L. Koppens, Nature (London) **487**, 77 (2012).

[3] Z. Fei, A. S. Rodin, G. O. Andreev, W. Bao, A. S. McLeod, M. Wagner, L. M. Zhang, Z. Zhao, M. Thiemens, G. Dominguez, M. M. Fogler, A. H. Castro Neto, C. N. Lau, F. Keilmann, and D. N. Basov, Nature (London) **487**, 82 (2012).

[4] M. Crommie, C. Lutz, and D. Eigler, Science **262**, 218 (1993).

[5] D. Subramaniam, F. Libisch, Y. Li, C. Pauly, V. Geringer, R. Reiter, T. Mashoff, M. Liebmann, J. Burgdörfer, C. Busse, T. Michely, R. Mazzarello, M. Pratzer, and M. Morgenstern, Phys. Rev. Lett. **108**, 046801 (2012).

[6] S. K. Hämäläinen, Z. Sun, M. P. Boneschanscher, A. Uppstu, M. Ijäs, A. Harju, D. Vanmaekelbergh, and P. Liljeroth, Phys. Rev. Lett. **107**, 236803 (2011).

[7] S.-H. Phark, J. Borme, A. L. Vanegas, M. Corbetta, D. Sander, and J. Kirschner, ACS Nano **5**, 8162 (2011).

[8] M. Kralj, I. Pletikosić, M. Petrović, P. Pervan, M. Milun, A. T. N'Diaye, C. Busse, T. Michely, J. Fujii, and I. Vobornik, Phys. Rev. B **84**, 075427 (2011).

[9] I. Pletikosić, M. Kralj, P. Pervan, R. Brako, J. Coraux, A. T. N'Diaye, C. Busse, and T. Michely, Phys. Rev. Lett. **102**, 056808 (2009).

[10] S. J. Altenburg, J. Kröger, T. O. Wehling, B. Sachs, A. I. Lichtenstein, and R. Berndt, Phys. Rev. Lett. **108**, 206805 (2012).

[11] A. Varykhalov, D. Marchenko, M. R. Scholz, E. D. L. Rienks, T. K. Kim, G. Bihlmayer, J. Sanchez-Barriga, and O. Rader, Phys. Rev. Lett. **108**, 066804 (2012).

[12] D. Niesner, T. Fauster, J. I. Dadap, N. Zaki, K. R. Knox, P.-C. Yeh, R. Bhandari, R. M. Osgood, M. Petrovic, and M. Kralj, Phys. Rev. B **85**, 081402 (2012).

[13] M. Pratzer and M. Morgenstern (private communication).

[14] I. Pletikosić, M. Kralj, D. Sokčević, R. Brako, P. Lazić, and P. Pervan, J. Phys.: Condens. Matter **22**, 135006 (2010).

[15] L. Petersen and P. Hedegård, Surf. Sci. **459**, 49 (2000).

[16] E. Grånäs, J. Knudsen, U. A. Schröder, T. Gerber, C. Busse, M. A. Arman, K. Schulte, J. N. Andersen, and T. Michely, ACS Nano **6**, 9951 (2012).

[17] R. Larciprete, S. Ulstrup, P. Lacovig, M. Dalmiglio, M. Bianchi, F. Mazzola, L. Hornekaer, F. Orlando, A. Baraldi, P. Hofmann, and S. Lizzit, ACS Nano **6**, 9551 (2012).

[18] R. M. Feenstra, J. A. Stronscio, and A. P. Fein, Surf. Sci. **181**, 295 (1987).

[19] M. Morgenstern, Surf. Rev. Lett. **10**, 933 (2003).

[20] I. Horcas, R. Fernández, J. M. Gómez-Rodríguez, J. Colchero, J. Gómez-Herrero, and A. M. Baro, Rev. Sci. Instrum. **78**, 013705 (2007).

[21] J. Coraux, A. T. N'Diaye, M. Engler, C. Busse, D. Wall, N. Buckanie, F.-J. Meyer zu Heringdorf, R. van Gastel, B. Poelsema, and T. Michely, New J. Phys. **11**, 023006 (2009).

[22] P. Hohenberg, Phys. Rev. **136**, B864 (1964).

[23] W. Kohn and L. J. Sham, Phys. Rev. **140**, A1133 (1965).

[24] G. Kresse and J. Furthmüller, Phys. Rev. B **54**, 11169 (1996).

[25] G. Kresse and J. Hafner, Phys. Rev. B **49**, 14251 (1994).

[26] P. E. Blöchl, Phys. Rev. B **50**, 17953 (1994).

[27] J. P. Perdew, K. Burke, and M. Ernzerhof, Phys. Rev. Lett. **77**, 3865 (1996).

[28] S. Grimme, J. Comput. Chem. **27**, 1787 (2006).

[29] S. Hüfner, *Photoelectron Spectroscopy: Principles and Applications*, *Advanced Texts in Physics* (Springer, Berlin, Heidelberg, 2003).

[30] Y. Yang, S. C. Wu, F. Q. Liu, K. Ibrahim, H. J. Qian, S. H. Lu, and F. Jona, Phys. Rev. B **54**, 5092 (1996).

[31] P. Kowalczyk, M. Puchalski, W. Kozłowski, P. Dąbrowski, Z. Klusek, and W. Olejniczak, Appl. Surf. Sci. **254**, 4572 (2008).

[32] C. Busse, P. Lazić, R. Djemour, J. Coraux, T. Gerber, N. Atodiresei, V. Caciuc, R. Brako, A. T. N'Diaye, S. Blügel, J. Zegenhagen, and T. Michely, Phys. Rev. Lett. **107**, 036101 (2011).

[33] F. Craes, S. Runte, J. Klinkhammer, M. Kralj, T. Michely, and C. Busse, Phys. Rev. Lett. **111**, 056804 (2013).

[34] K. Schouteden, E. Lijnen, E. Janssens, A. Ceulemans, L. F. Chibotaru, P. Lievens, and C. V. Haesendonck, New J. Phys. **10**, 043016 (2008).

[35] A. H. Castro Neto, F. Guinea, N. M. R. Peres, K. S. Novoselov, and A. K. Geim, Rev. Mod. Phys. **81**, 109 (2009).

[36] Y. Zhang, V. W. Brar, F. Wang, C. Girit, Y. Yayon, M. Panlasigui, A. Zettl, and M. F. Crommie, Nat. Phys. **4**, 627 (2008).

[37] G. M. Rutter, J. N. Crain, N. P. Guisinger, P. N. First, and J. A. Stroscio, Science **317**, 219 (2007).

[38] P. Mallet, I. Brihuega, S. Bose, M. M. Ugeda, J. M. Gómez-Rodríguez, K. Kern, and J. Y. Veuillen, Phys. Rev. B **86**, 045444 (2012).